JGR Space Physics

RESEARCH ARTICLE
10.1029/2019JA027596

Suprathermal Fe in the Earth's Plasma Environment: Cluster RAPID Observations

S. Haaland[1,2], P. W. Daly[1], E. Vilenius[1], P. Krcelic[1,3], and I. Dandouras[4]

[1]Max-Planck Institute for Solar Systems Research, Göttingen, Germany, [2]Birkeland Centre for Space Science, University of Bergen, Bergen, Norway, [3]Department of Geophysics, University of Zagreb, Zagreb, Croatia, [4]Institut de Recherche en Astrophysique at Planetologie, Université de Toulouse/CNRS/UPS/CNES, Toulouse, France

Key Points:
- We present the first observations of (Fe^{+}/Fe^{N+}) from the Cluster mission
- Suprathermal Fe is detected in all regions traversed by Cluster
- Time variations and likely sources of the observed Fe ions are investigated

Correspondence to:
S. Haaland,
Stein.Haaland@uib.no

Citation:
Haaland, S., Daly, P. W., Vilenius, E., Krcelic, P., & Dandouras, I. (2020). Suprathermal Fe in the Earth's plasma environment: Cluster RAPID observations. *Journal of Geophysical Research: Space Physics*, *125*, e2019JA027596. https://doi.org/10.1029/2019JA027596

Received 4 NOV 2019
Accepted 17 JAN 2020
Accepted article online 3 FEB 2020

Abstract Baryonic matter in geospace is almost exclusively in a plasma state, with protons (H^{+}) and to some extent ionized helium (He) and oxygen (O) being the dominant ion species. But also other heavier ion species and even molecular ions are present in geospace. The Research with Adaptive Particle Imaging Detectors (RAPID) on board the Cluster satellites can identify and characterize some of these ions by utilizing their measured time of flight and energy. Usually, the measurements are then assigned into three discrete species channels; protons (H^{+}), helium (He), and a common channel for carbon, nitrogen, and oxygen (CNO), each with flux, energy, and angular information. But RAPID also has a Direct Event (DE) diagnostic mode in which the full time of flight and energy information for a limited number of incident particles are stored. With knowledge about energy losses in the various detector parts, it is then possible to derive the atomic mass of the incident particle. In this paper we report on results from a study of Cluster DE events during the years 2001–2018, with a particular emphasis of iron (Fe) ions. We show that suprathermal Fe ions can be found all over geospace covered by Cluster, and that the time variation is consistent with modulation by geomagnetic disturbances and solar activity. We do not find any clear correlations between detection of suprathermal Fe and meteor showers or sputtering off the moon.

1. Introduction

In geospace, protons and to some extent helium (He) and oxygen (O) ions are the dominant ion species and thus most relevant for the electrodynamics of the magnetosphere and ionosphere. But also other, heavier ion species and even molecular ions are present in geospace. Molecular ions are predominantly of terrestrial origin (Dandouras et al., 2019; Christon, 2019; Yau et al., 1993), whereas the sources of other heavy ions and their relative contribution is still debated. In this paper, we present Cluster observations of iron (Fe), which has an atomic mass around 56 atomic mass units (AMU) in its most frequently occurring isotope. We investigate the occurrence rates of Fe as a function of plasma region and variations of the Fe detection in response to geomagnetic activity and solar cycle variations. For the rest of this paper, we use the notation Fe^{N+} for higher charge states (where N indicates the charge state), Fe^{+} for single ionized iron, and just Fe for iron in general.

A known source of Fe is the solar wind, the composition of which is a mixture of materials found in the solar corona. Ionized hydrogen (protons) dominate together with an approximately 4% He content (Geiss et al., 2004; Neugebauer, 1981; Rakowski & Laming, 2012) and traceable amounts of other heavy ions and atomic matter. The first detection of heavy ions, including Fe, in the solar wind was made with the Vela spacecraft in the late 1960s (Bame, 1970). Later, measurements from the Ulysses and SOHO spacecraft (Galvin et al., 1996; von Steiger et al., 1997) found traces of carbon (C), nitrogen (N), oxygen, neon (Ne), magnesium (Mg), silicon (Si), and sulfur (S) typically stripped of their valence electron and thus of high charge states. Plasma of solar wind origin can enter the magnetosphere through magnetic reconnection (Paschmann et al., 1979) or diffusive processes (Treumann, 1997) or direct entry through the cusp (Shi et al., 2013) (see also overview in, e.g., Hultqvist & Øieroset, 1997). Observations have shown that also Fe of solar wind origin can enter the magnetosphere directly via the cusp (Fritz et al., 2003) and mix with any preexisting Fe.

Outflow from the terrestrial ionosphere is another important source of ions in geospace (Shelley et al., 1972; Yau & Andre, 1997). Every day, the Earth's atmosphere loses hundreds of tonnes of material into space through outflow of both neutrals and ions. The escape of atmospheric material is not unique to the Earth

but is a fundamental process and takes place also on other planets, moons, asteroids, and comets (Yamauchi & Wahlund, 2007). In Earth's geospace, ions of ionospheric origin are a significant or even dominant source of plasma to the magnetosphere (Chappell, 1987). Protons and oxygen are the dominant species of terrestrial outflow. So far, there has been less focus on the outflow of heavier ions, partly due to lack of proper instrumentation to separate species in the more recent spacecraft missions, and partly because the impact on magnetospheric dynamics is probably negligible for other species.

The ionospheric source of Fe^+ (i.e., singly ionized iron) is primarily debris caused by meteoroid and meteor impact and subsequent ablation in the Earth's atmosphere (Christon et al., 2017; Plane, 1991). During the ablation process, metallic ions are formed by impact ionization and deposited in layers of the mesosphere at around 90–100 km altitude (Plane et al., 1999). There are also reports of detection of neutral Fe at higher altitudes (Chu, 2011). Whereas the presence of Fe ions in the atmosphere is established, there are few studies on how these ions can be extracted from the mesospheric layers through the upper ionosphere into space. Due to their mass, Fe is stronger gravitational bound, and many of the classical outflow mechanisms, for example, acceleration by ambient electric fields, transverse heating, and subsequent increase in the mirror force or other thermal forces (Yau & Andre, 1997), are less effective.

In space, sputtering (i.e., ejection of Fe from the surface due to bombardment by energetic particles in the solar wind or microscale dust particles) and ablation from asteroids are also sources of Fe (Nakamura et al., 2012; Popova et al., 2007). A special case near Earth is sputtering from the Moon. The lunar surface contains a significant fraction of iron oxide (FeO), already noted by the Apollo astronauts during their exploration of the lunar surface (Agrell et al., 1970; Baron et al., 1977; Korotev, 1997). Sputtering off the moon by solar wind incidence has been suggested to be a source of Fe for the magnetosphere (Hapke, 1973; Pillinger et al., 1976; Poppe et al., 2016; Wurz et al., 2007), the but resulting Fe flux and their possible impact on the magnetosphere has not been studied in very much detail.

The paper is organized as follows. In section 2, we give an overview of the Cluster mission, its orbit, and instrumentation used. In section 3, we present Fe occurrence rates for the various regions of space covered by Cluster. Section 4 discusses sputtering of the lunar surface and asteroids as a possible source of the detected Fe. Section 5 discusses long time temporal variations in the Fe detection rate due to changes in the solar wind and possible detector degradation. Finally, section 6 summarizes the main results of this investigation.

2. Data and Analysis and Technique

The main results presented in this paper are based on measurements by the Research with Adaptive Particle Imaging Detectors (RAPID; see Wilken et al., 1997, 2001) instrument on board the Cluster satellites over the time period 2001–2018.

Cluster is a constellation of four identical spacecraft launched in 2000 into a high inclination 4×19 Re polar orbit (Escoubet, 1997). The apogee of Cluster is in the Earth's magnetotail around September equinox and in the solar wind around March equinox (the orbit changes slightly over time due to natural perturbations and/or spacecraft maneuvers, but this is not of importance for the present study). With this orbit, Cluster provides extended coverage of all key regions of geospace within a year, the solar wind and upstream bow shock regions, the magnetosheath, the high-latitude cusp and polar regions, the flank magnetopause and boundary layers, and the magnetotail lobes as well as the nightside tail plasma sheet.

Each of the four Cluster satellites carries a comprehensive set of instrumentation, including the RAPID energetic particle detector used for the present study. In the scientific literature, the four spacecraft are simply referred to as SC1, SC2, SC3, and SC4, and we will use this notation hereafter. Each spacecraft has a nominal spin period of about 4 s, and a telemetry capacity of about 17 kbit/s distributed among the instruments. Measurements are taken either in nominal (low-bit-rate) or burst (high-bit-rate) modes. As shown below, the limited storage capacity and telemetry rates put some limitations on our ability to detect and characterize heavy ions.

2.1. Detection Principle—RAPID and Direct Events

Relevant for the present study is the energy and time-of-flight measurements from the RAPID Imaging Ion Mass Spectrometer (IIMS), schematically illustrated in Figure 1. IIMS consists of three identical Spectroscopic Camera for Electrons, Neutrals and Ion composition (SCENIC) heads, each covering a 60° polar angle. When operated to get fluxes or distribution functions, the spacecraft spin (period ~4 s) is utilized to

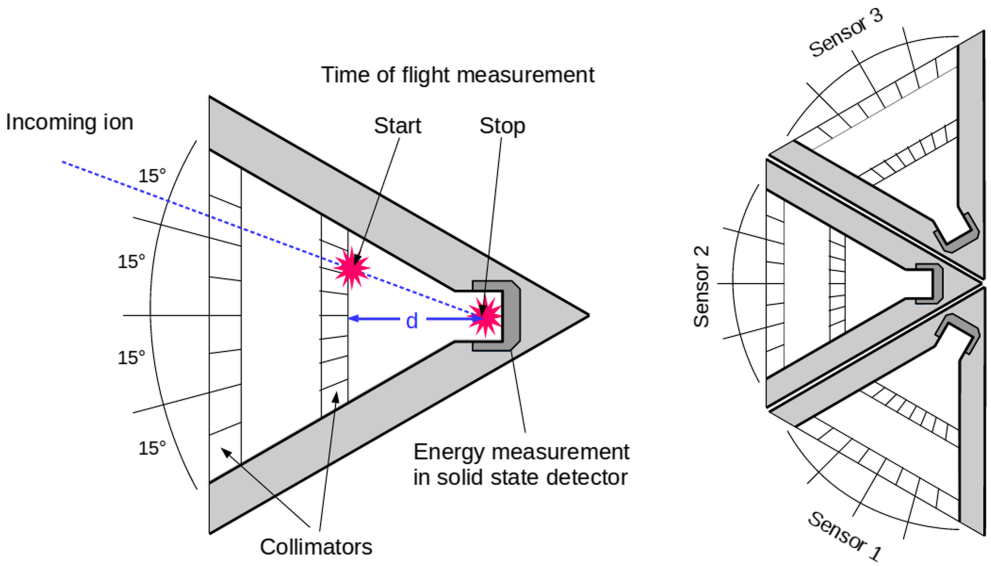

Figure 1. (left) Schematic illustration of a single SCENIC IIMS sensor head. A start signal is generated by electrons emitted when the incoming ion passes the start foil, and a stop signal is generated by electrons when the ion hits the surface of the solid state detector. The emitted electrons are detected by microchannel plate detectors under high voltage. From the known travel distance (d = 32–37 mm, depending on incidence angle), the velocity of the ion can be detected. Combined with the energy, the ion species (but not their charge state) can be determined. (right) Illustration of three SCENIC heads combined to cover 0–180° elevation.

get the full 3-D distribution function of the species H, He, and CNO (carbon, nitrogen, and oxygen—which have indistinguishable masses—see below).

The particle identifying function of IIMS relies on the particle's velocity (V) and energy (E). From this, the particle mass, M, can be uniquely determined either by the computation ($M \propto E/V^2$) or by statistical analysis in two-dimensional (V, E) space with the mass M as the sorting parameter. The velocity is determined from the flight time (T) the particle needs to travel a known distance, d_{TOF} in the detector geometry, and the energy is determined from the solid state detector pulse height. We will hereafter refer to this combination of energy and time of flight simply as E-TOF.

The mass resolution enables the distinction between various ion species but, as noted above, is not sufficient to distinguish between nitrogen (N), oxygen (O), and carbon (C) which have very similar atomic masses. This data product from RAPID is therefore frequently referred to as CNO. For the same reason, we are not able to distinguish between different isotopes of a particular ion species.

Whereas the regular ion telemetry products on RAPID deliver count rates (and, thanks to calibration, ensuing fluxes) and up to eight broad energy channels for each of the three species (H, He, CNO), the Direct Event (DE) product provides the full information on the energy deposited in the solid state detector for the events (256 energy bins, representing energies between approximately 30 keV to 4 MeV) and the time of flight (80 ns in 256 bins), but only for a limited number of events (detected ions) due to constraints in telemetry. With both energy, velocity as well as direction of incidence, RAPID DEs thus offer a window into the high mass regions, for example Si and Fe.

Due to its role as a diagnostics tool rather than a science product, the DE data product has a few caveats that needs to be taken into account. First, unlike, for example, the Cluster Ion Spectrometry (see Rème et al., 2001) onboard Cluster, RAPID does not apply any electrostatic deflection to determine charge state, nor any preacceleration or postacceleration to compensate for energy losses in the foils. The energy threshold is rather high: An incoming ion will first hit the start foil of the detector system and loose some of its initial energy. The loss of energy will depend on both initial energy, species and angle of incidence. In general, heavier ions will have larger energy losses. A second energy loss occurs in the solid state detector itself. Based on early simulations of losses in the start/stop foils and solid state detector of RAPID IIMS, an incoming Fe ion needs approximately 400 keV in order to produce a valid E-TOF signal.

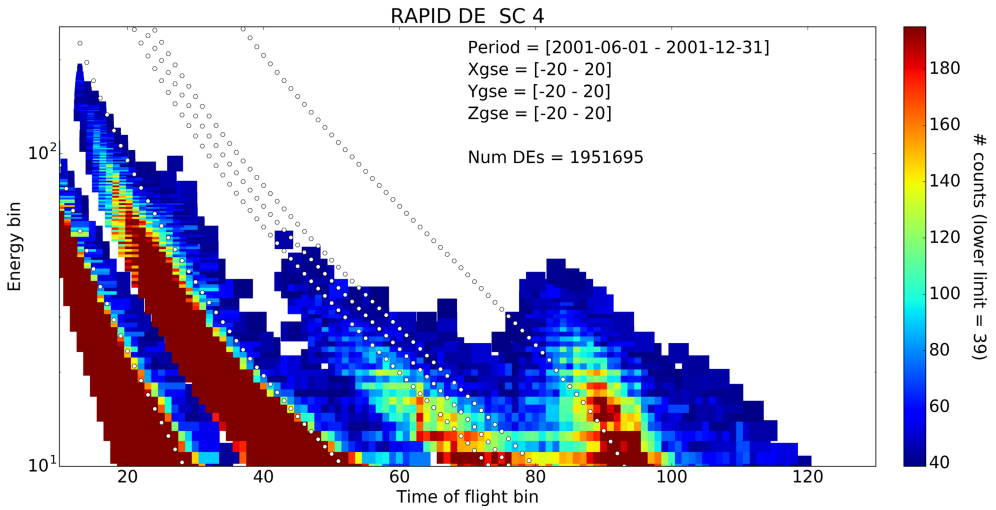

Figure 2. Energy versus time-of-flight map from the RAPID IIMS sensor on board Cluster SC4. This map is generated by accumulating all DEs during the first half year of science operations. Four distinct populations can easily be identified; H, He, CNO, and Fe. The colors show count rates, but due to the priority scheme described in section 2.1, colors cannot be used to say anything about the ratio between species (and H and He are saturated to emphasize the heavier ions), or calibrated fluxes. White lines indicate theoretical energy versus time of flight (E-TOF) for six major species; H, He, C, N, O, and Fe. The low-energy spill-over around TOF bins 80–90 may be molecular ions.

All instruments on board Cluster undergo regular cross calibrations (Laakso et al., 2010), but this does not apply to the DE results. Thus, no comprehensive studies or corrections for sensor degradation and its response to Fe ions over time have been conducted for DEs. The central head (Sensor Head 2 in the illustration in Figure 1) of RAPID degraded rapidly early in the mission (Daly & Kronberg, 2019), presumably due to sunlight contamination. Consequently, very few DEs from this sensor head are available after 2001, and our ability to infer directional information is constrained.

As seen in Figure 1, the polar angular resolution is approximately 15°. This means that the time-of-flight path can vary between 32 and 37 mm, thus introducing an uncertainty of 15% or more in the determination of the velocity, and consequently mass determination. An additional degradation of the instrument mass resolution comes from the stochastic nature of the ion path through the start foil, with multiple scattering across successive atomic layers. This introduces a broad distribution of the exit velocities from the foil, even for ions having the same initial energy, mass and incidence angle. Ions with a given mass (i.e., a specific ion species) will thus occupy a band rather than a single line in the E-TOF parameter space. Note that the working principle of IIMS also does not allow any charge state discrimination.

A third drawback to the DE product is that for reasons of limited on board storage and telemetry bandwidth, only 20 complete DE records per spin can be transmitted in nominal mode, and 106 records per spin in burst mode. Although a priority scheme ensures that the rarer events (heavier ions) are transmitted first, it is not possible to reproduce count rates or fluxes from the DE product. Note also that in the initial years of the Cluster mission, only about 50% of the science data were being downloaded. Starting in 2003, additional ground telemetry stations were made available for the mission, and it was decided to download data from all times. Except for planned maneuvers and scheduling, eclipses and occasional instrument reboots or failures, a near 100% planned data return has been achieved in later years.

Figure 2 shows how Fe (atomic mass around 56 AMU for the most abundant isotope) emerges as a distinct population between time-of-flight bins 90 and 100 in the E-TOF map. Since the energy threshold is different for different species, we show energy bin numbers rather than energy along the vertical axis (the lower range, bin 10, corresponds to approximately 65 keV for protons). This map is generated by accumulating DE measurements from the RAPID instrument on SC4 over the first 6 months of Cluster operation, and thus cover all regions of space (but with the majority of the time spent inside the magnetosphere in the high-latitude polar areas and magnetotail lobe regions).

White dashed lines indicate the theoretical E-TOF values assuming direct impact (i.e., the shortest possible flight distance $d_{TOF} = 32$ mm in Figure 1 with no geometry distortions). Later in this paper, we will also

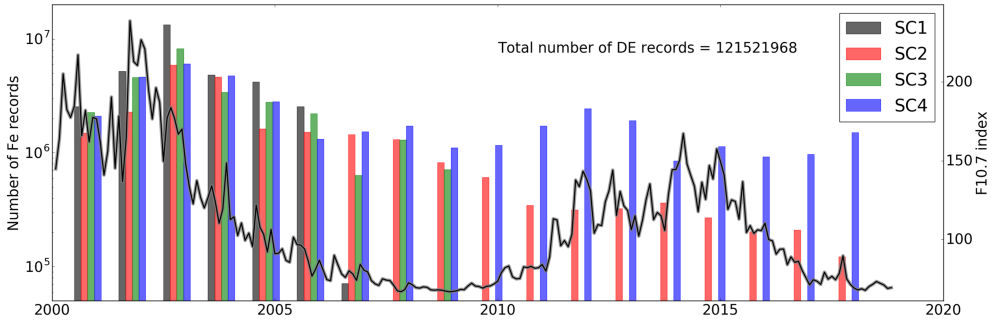

Figure 3. Overview of data from the four Cluster spacecraft. Direct events are available from June 2001 until 2019 for SC2 and SC4, but only until early 2007 for SC1 and early 2009 for SC3. The black curve overlaid shows the F10.7 index—a proxy for solar activity, further discussed in section 5.

introduce a second line corresponding to the longest possible flight distance (d_{TOF} = 37 mm), and identify Fe by E-TOF combinations between these two lines. The calibration lines are based on simulations of sensor responses using Stopping and Range of Ions in Matter (SRIM) simulations (Ziegler et al., 2010) to estimate energy losses in thin foils and solid state detectors, and assuming that the estimated energy losses in the start/stop foils and solid state energy detector do not change over time.

Given the fairly coarse mass resolution of the RAPID instrument, one could argue that the observations in the 90–100 bin TOF range could be any ion species or isotope with masses between approximately 40 and 70 AMU. However, the reported abundances of isotopes other than Fe within this mass range are much lower in the regions of space relevant for the present study (Jarosewich, 1990; Manuel & Hwaung, 1983; von Steiger et al.,1997, 2000). Molecular ions such as N_2, CO, NO, and O_2, sometimes found in the magnetosphere as a result of ion outflow (Christon, 2019; Yau et al., 1993) have atomic masses in the range 28–32 and should show outside the Fe interval in the E-TOF map.

In the on board algorithms, E-TOF calculations are used internally to assign each measurements into one out of four species groups (H, He, CNO, and "heavy ions") and eight energy channels. Together with angular information and spin phase, this classification is used to construct 3-D distribution functions of H, He, and CNO (but not for "heavy ions"). Only these 3-D distributions are sent via telemetry to ground and (after ground calibration and some processing) available as standard science data products from RAPID.

2.2. Overview of Data

By the time of writing, RAPID is still in operation on all spacecraft, but DE results are available from SC1 only until 2007, and for SC3 until 2009. Coverage details along with solar activity are shown in Figure 3. In general, DE data are available whenever RAPID is in operation, that is, essentially all the time except for spacecraft maneuvers or eclipses. We will hereafter focus on measurements from SC4, which has the best coverage with almost continuous measurements from 2001 to 2018. This period corresponds to the peak of solar cycle 23 and almost the complete solar cycle 24.

We have stored each individual DE from all four spacecraft in a relational database. Stored quantities from each Cluster spacecraft are: date and time, the polar look direction, the spin sector, the time-of-flight bin (0..255, corresponding to 0–80 ns), the energy bin (also 0..255) and Cluster spacecraft position. Information about solar wind, IMF, solar illumination (the F10.7 index), and geomagnetic activity is stored in a second table in this database. A third table contains the moon position and its magnetic connection to Cluster as well as information about time and position of meteor swarms throughout Earth's orbit around the Sun (see section 4).

2.3. Estimating Fe Occurrence Rates

As noted by Christon et al. (2017), Fe is a very rare species in geospace. In their Figure 4, which shows the correlation between solar activity and Fe^+ abundance, they show Fe^+ count rates around 10^{-3} to 10^{-2} per 3 hr interval, that is, 10^{-7} to 10^{-6} counts/second. Obviously, these count rates are based on accumulations over much longer time periods. Even in the solar wind, only about every 10^{-6} ion is an Fe ion (Mitchell et al., 1983; von Steiger et al., 2000). For the technical reasons explained above, it is not possible to calculate fluxes or count rates of Fe ions from the RAPID DE mode, so we are not able to compare to these numbers. As a

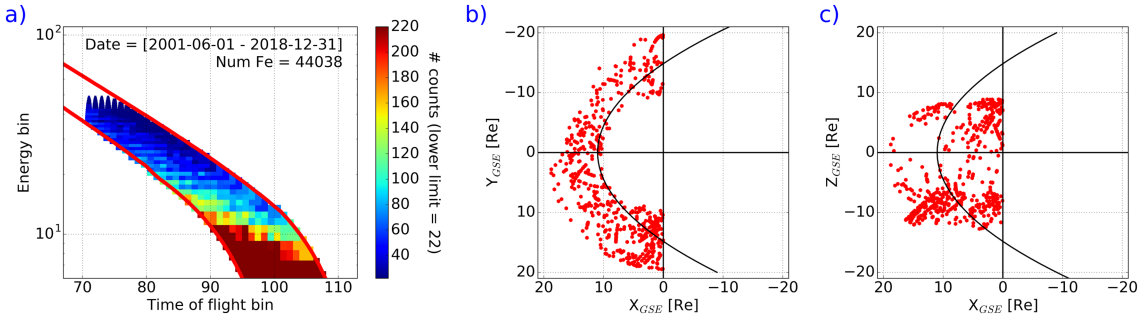

Figure 4. Cluster RAPID Fe detection in the solar wind and upstream bow shock/magnetosheath region (i.e., outside the static model magnetopause). (a) Zoomed-in version of the E-vs-TOF map from Figure 2. Red lines delineate the Fe region, that is, ions with atomic mass 56 and incidence angles between 0° (leftmost line, corresponding to shortest TOF) and 30° (rightmost line, longest TOF). (b and c) XY_{GSE} and XZ_{GSE} projections of the magnetosphere with Fe observations marked by a red dot.

proxy for Fe abundance, we therefore calculated occurrence rates, that is, the percentage of time when Fe is detected by RAPID.

Estimating occurrence rates is done as following: We first accumulate all DE events over an extended time period from a specific plasma region (see section 3) or for a specific condition (e.g., when the Moon is inside the magnetosphere) and group the observations into 1 hr intervals. From the E-vs-TOF map, we then isolate the Fe events, by only considering values in the E and TOF parameter space consistent with Fe. If at least six DEs consistent with Fe are recorded within a 1 hr block, we consider it a positive Fe observation and record its position. The threshold of six DEs per hour is somewhat randomly selected, but the purpose is to avoid that random noise and spurious start/stop signals are counted as valid Fe detections. We define the percentage of 1 hr blocks with positive Fe observations as the *occurrence rate*.

3. Fe Occurrence Rate by Region

We now investigate the Fe occurrence rate as described above in various regions of space. As in Christon et al. (2017) we define the various regions of space according to simple models and spatial locations. A more elaborate approach using combinations of plasma beta, spacecraft charge or other measured field and plasma properties to identify the plasma region (Baumjohann, 1988; Baumjohann et al., 1989; Eastwood, 2015; Haaland et al., 2009) was considered, but abandoned since such parameters were not always possible or consistent over the entire Cluster period (Boakes et al., 2014).

When comparing regions below, we accumulate Fe DEs over the entire observational period—mid 2001 to the end of 2018 without any filtering for geomagnetic activity, solar wind condition or solar activity. The definition of regions is fairly conservative (i.e, we have tried to exclude any boundaries between different plasma regions), and we anticipate that "contamination" by observation from adjacent regions is minimal.

Cluster, with its 4 × 19 Re polar orbit and long time of observations, provide opportunities to investigate the Fe abundance in the following regions: (1) the solar wind and upstream magnetosheath region; (2) the high-latitude polar cap and cusp regions in both hemispheres; (3) the magnetotail lobes; (4) the tail plasma sheet out to Cluster's apogee around 19 Re; and (5) the inner magnetosphere.

3.1. Fe in the Solar Wind and Upstream Region

Figure 4a shows the E-vs-TOF map and locations of Fe encounters in the upstream magnetosheath and solar wind region, defined as all dayside positions outside a static parabolic model magnetopause (Fairfield, 1971) with a 13 Re standoff distance at noon. Figures 4b and 4c show the GSE (Geocentric Solar Ecliptic) locations where Fe was detected, each observation indicated by a red dot. Cluster SC4 spent a total of 34,870 hr in this region with the DE mode active. Fe was encountered during 2,030 1 hr intervals, corresponding to approximately 6% of the total observation time.

The solar wind is known to be a source of Fe (Grevesse, 1984; von Steiger et al., 2000), so the rather high percentage of time in which Fe is observed is not surprising. Furthermore, it is reasonable to assume that most of the observed ions in this region are high charge state $Fe^{6+/16+}$ (Galvin et al., 2009; Heidrich-Meisner et al., 2016; von Steiger et al., 2000), and that a substantial part of their energy is a consequence of the high ram

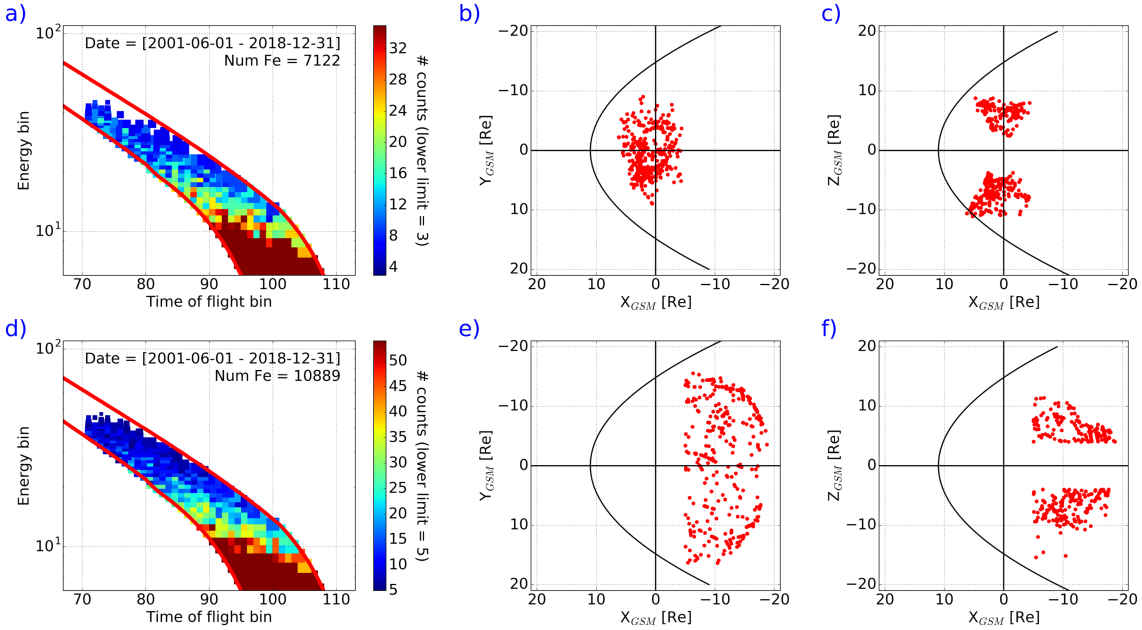

Figure 5. Similar to figure 4, but for the high-latitude polar cap region and lobes. (a to c) The E-TOF map and locations of Fe detection in the high-latitude polar caps, defined as any Cluster GSM position poleward of 60° in both hemispheres. (d to f) The corresponding E-TOF and locations of Fe detection in the magnetotail lobes, defined by a spatial volume limited by $X_{GSM} \leq -5$ Re, $|Y|_{GSM} \leq$ 15 Re, and $|Z|_{GSM} \geq 5$ Re.

velocity in the solar wind and magnetosheath (Bochsler et al., 2010). Leakage of energetic ions from the magnetosphere into the magnetosheath (sometimes referred to as *upstream events* Asbridge, 1968; Sibeck et al., 1987) can not be excluded, but this population is obviously difficult to distinguish from solar wind ions in our measurements.

3.2. Fe in the High-Latitude Polar Cap and Magnetotail Lobes

We now focus on Fe detection inside the magnetosphere, and use the Geocentric Solar Magnetospheric (GSM) coordinate system to define locations. The polar ionosphere is known to be an important source of plasma to the magnetosphere (Chappell, 1987), and Christon et al. (2017) focused on Fe^+ of mesospheric and ionospheric origin. In their study, the transport of these Fe^+ ions into the magnetosphere was not discussed in any detail, but typically, ions escaping from the high-latitude ionosphere are accelerated by a combination of the mirror force (Seki et al., 2002), field aligned ambient electrical field (Banks & Holzer, 1968) and to some extent centrifugal forces (Cladis, 1986). In the absence of collisions above the exobase, ions are magnetized and travel outward along open *B* field lines. This transport path will take the ions up through the high-latitude cusp or polar cap regions. A substantial part of the outflowing plasma will continue downtail through the magnetotail lobes where additional field aligned acceleration due to centrifugal acceleration and convection will take place (Nilsson et al., 2008).

The top part of Figure 5 shows the E-TOF map and locations around the cusp and high-latitude polar regions where Fe was detected. In our model, the high-latitude/cusp region is simply defined GSM latitudes poleward of 60° in both hemispheres, but with no limit on altitude (other than the limits given by the orbit of Cluster). In reality, the size, shape and location of the open polar cap and cusp can vary significantly with solar wind conditions and geomagnetic activity, but our simple model still gives an indication of Fe in this region.

In total, 13,448 hr of DE observations were available from SC4 in the high-latitude polar cap and cusp regions in both hemispheres. Fe was detected during 184 hr, corresponding to approximately 1.4% of the time, that is, considerably less frequent than in the solar wind. Possible reasons for this will be discussed in section 3.4.

Figures 5d–5f show the corresponding E-TOF map and locations of Fe in the magnetotail lobes. The magnetotail lobes are magnetically connected to the high-latitude polar cap region in one end and the downtail interplanetary magnetic field in the other end. They are characterized by a very low plasma density and predominantly sunward and/or tailward directed magnetic field. Ideally, we would have delineated the lobes

using plasma beta or other proxies, but as noted above, estimations of plasma beta in this region is difficult due to spacecraft charging effects and low count rates (Boakes et al., 2014; Haaland et al., 2009). Lobes in this paper are therefore conservatively defined by the locations $X_{GSM} \leq -5$ Re; $|Y|_{GSM} \leq 15$Re and $|Z|_{GSM} \geq 4$ Re.

Outflow from the ionosphere is subject to a velocity filter effect: During low to moderate geomagnetic activity with little or no convection, a substantial part of ions escaping from the polar cap regions (presumably including any Fe^+ of mesospheric origin) will traverse the lobe regions. During periods with higher geomagnetic activity and stronger convection, a substantial part of plasma escaping from the polar cap is convected to the central plasma sheet close to Earth, that is, inside Cluster's apogee and thus undetected. Strong wave-related acceleration and/or centrifugal acceleration will modify this velocity filter effect (Lundin & Guglielmi, 2006). Some heavy ions and very energetic ions from the dayside polar cap region and cusp will also escape directly into the magnetosheath and plasma mantle regions (Slapak et al., 2015, 2017).

In addition to a possible terrestrial source of Fe in the lobes, sputtering off the lunar surface may also be a source of heavy ions in this region. Tanaka et al. (2009) reported observations from the Plasma energy Angle and Composition Experiment (PACE) onboard the Kaguya lunar explorer spacecraft when the Moon was in the magnetotail lobes. Although they did not mention Fe explicitly, they pointed out that the absence of any strong acceleration mechanisms or plasma processes in the lobe region, enabled them to detect even small abundances of ions of lunar origin.

Our data set contains 21,977 hr of DE observations from the lobes as defined above. Fe was detected during 321 hr, corresponding to 1.5% of the time. This occurrence rate is comparable to that found in the cusp and polar cap region, but much lower than the in solar wind. A possible explanation is discussed in section 3.4.

3.3. Fe in the Tail Plasma Sheet and Inner Magnetosphere

Large scale magnetospheric convection ensures that most of the plasma supplied from both the ionosphere and the solar wind are transported through the lobes to the nightside magnetotail from both hemispheres. Consequently, a sheet of dense plasma is formed—the central plasma—with peak density near the GSM ecliptic. Various heating processes (Hultqvist & Stenflo, 1975; Hoshino et al., 1997; Lyons & Speiser, 1982) thermalize and heat the plasma and can accelerate particles to high energies. Outflow and transport of Fe from the ionosphere or solar wind can therefore be expected to show up also in the nightside plasma sheet. Transport time of plasma from the ionosphere to the plasma sheet depends on the convection velocity and field aligned velocity of the outflowing ions, and can be several hours.

Inward convection and adiabatic energization (Baumjohann, 1998; Ebihara & Ejiri, 2003) combined with impulsive Earthward acceleration events (injections; see e.g., McIlwain, 1974) will transport much of the nightside plasma sheet plasma toward the Earth. Consequently, the plasma density and plasma pressure is even higher in the inner magnetosphere than in the tail plasma sheet further downtail. Gradient and curvature drift will eventually divert the plasma around the flanks and to the dayside magnetosphere. The ring current—set up by energetic ions and electrons drifting in opposite direction is known to contain significant amounts of heavy ions (in particular O^+) of ionospheric origin (Kronberg et al., 2014; Yau et al., 2012).

Cluster, with its polar orbit, crosses the nightside plasma sheet near apogee from approximately August to November. Due to the polar orbit, Cluster does not spend as much time in this region as, for example, the GEOTAIL spacecraft used by Christon et al. (2017) or the later THEMIS (Angelopoulos, 2008) satellites with their ecliptic orbits. In our simplified model, the nightside plasma sheet is constrained by $X_{GSM} \leq$-5Re, Y_{GSM} within ±15 Re and Z_{GSM} withing ±4 Re. Figure 6a–6c show the E-TOF map and the locations where Fe was detected in the nightside plasma sheet. Cluster SC4 recorded 9,632 hr of DEs, with 1,497 hr containing Fe ions, corresponding to 15% of the observation time.

The Fe occurrence rate in the inner magnetosphere is even higher. In our model, we somewhat arbitrarily define the inner magnetosphere as any location inside 6.6 Re radial distance (i.e., geosynchronous orbit), and limited by Cluster's orbit perigee (typically about 4 Re, but down to 2 Re in 2007–2008). Figures 6d–6e of show the corresponding E-TOF maps and locations of Fe detection. Cluster spent 11,937 hr in the inner magnetosphere region with DE operating, and Fe was observed during 3,812 hr, corresponding to 32% of the time. From Figure 6e we note a higher occurrence rate at dusk, consistent with the clockwise gradient- and curvature drift and various loss processes as the ions drift around the Earth.

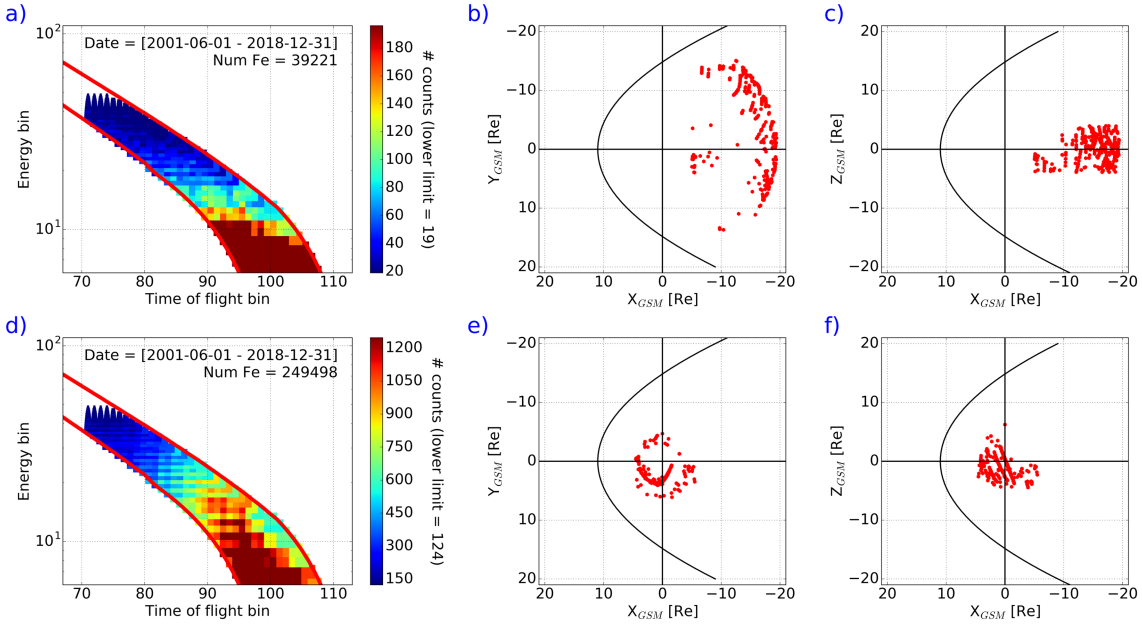

Figure 6. As in Figure 4, but for the nightside plasma sheet and inner magnetosphere. (a) E-TOF map for the nightside plasma sheet, defined by a spatial box with coordinates $X_{GSM} \leq -5$ Re, Y_{GSM} within ±15 Re, and Z_{GSM} within ±4 Re. Locations of Fe detection are shown in (c) and (d). Due to the polar orbit of Cluster, most of the plasma sheet crossings are near apogee around 19 Re radial distance during the period July–October each year. (d) The corresponding E-TOF map for the inner magnetosphere, here somewhat arbitrarily defined as geospace inside geosynchnronous orbit. As seen in the projections in (e) and (f), the perigee of Cluster at 4 Re means that only the outer parts of the ring current and radiation belts are covered.

Due to the above described priorization scheme and the lack of sensor calibration for Fe, it is not possible to derive meaningful energy spectra from DE observations. From the E-TOF map in Figure 6d, we note that there are higher count rates in the higher energy bins (higher energy) in the inner magnetosphere. This would indicate a hotter (more energetic) Fe population, consistent with the higher energies observed also for lighter ions.

3.4. Regional Differences in Fe Abundance

Table 1 summarizes the occurrence rates in the various regions investigated. For convenience, we also give the corresponding total rate, that is, all Fe events detected by Cluster SC4 during the years 2001–2018. We note that Cluster RAPID detects Fe in all regions covered, but occurrence rates varies strongly between the various regions. The highest occurrence rates and the highest concentrations are found in the plasma sheet and inner magnetosphere. These regions are also where the highest fluxes of energetic particles can be found, so this is perhaps not surprising.

The much lower occurrence rates in the polar cap and lobe regions can partly be explained by a detection issue; Due to energy system losses, for example, energy losses in the time of flight start foil and the solid state energy detector, RAPID IIMS has a set of lower detection threshold energies. For protons, this is about 28 keV as frequently cited in publications using RAPID. For Fe, the detector system losses are much higher and initial simulations (Ziegler et al., 2010) suggest that Fe ions need to have initial energies above 400 keV to be detected. In the solar wind, with its fast bulk speed (≈ 400 to 800 km/s), and in the plasma sheet and inner magnetosphere these energies are available due to a combination of ram energy (bulk flows can be 1,000 km/s or more—see, e.g., Angelopoulos et al., 1994) and thermal energy (essentially related to gyro motion of ions). In the polar cap region and the lobes, no strong acceleration mechanisms exist, and flow velocities and temperatures are much lower.

4. Other Sources: Fe From Lunar or Meteoric Sputtering

In addition to the solar wind and ionospheric origin, other potential sources for Fe in space are meteors (Abrahams & Nimmo, 2019) and the lunar surface (Colaprete et al., 2016; Poppe et al., 2016; Tanaka et al., 2009). The fundamental mechanism is the same: Sputtering (i.e., ejection of material) from a surface is

Table 1
Summary of Cluster SC4 DE Observations and Fe Occurrence by Region (Top Five Rows) and the Sum of All Detected Fe Events by Cluster SC4 During the Years 2001–2018 (Bottom Row)

Region	Definition of region	Time with DE observations (hr)	Time with Fe observations (hr)	Fe occurence (% of time)
Solar wind	Outside static model by (Fairfield, 1971)	34,870	2,030	5.8
High latitudes, polar cap and cusp	Poleward of 60° latitude	13,448	184	1.4
Lobe	$X_{GSM} \leq -5$ Re $\lvert Y\rvert_{GSM} \leq 15$ Re $\lvert Z\rvert_{GSM} \geq 4$ Re	21,977	321	1.5
Plasma sheet	$X_{GSM} \leq -5$ Re $\lvert Y\rvert_{GSM} \leq 15$ Re $\lvert Z\rvert_{GSM} \leq 4$ Re	9,632	1,497	15.6
Inner magnetosphere	Cluster inside 6.6 Re radial distance	11,937	3,812	31.9
Entire Cluster coverage	Sum of all SC4 Fe observation 2001–2018	122,609	11,915	9.1

caused by bombardment by energetic particles from the solar wind or microsscale dust particles. Some of this material will escape from the lunar or cometary body (Hapke, 1973; Pillinger et al., 1976; Saito et al., 2010; Wurz et al., 2007). In addition to evacuating of material from the surfaces, relevant for our Fe study, an important aspect of this process is obviously also that it changes the surface of the moon and asteroids, and contributes to their erosion (Kuhlman, 2015).

4.1. The Moon as a Source of Magnetospheric Fe

The lunar surface contains a significant fraction of Fe, mostly in the form of iron oxide (FeO) molecules. To check whether sputtering off the lunar surface can produce any detectable Fe in the magnetosphere, we isolated all periods when the Moon was inside the magnetopause (i.e, traversing the tail of the magnetosphere within $Y_{GSE} \pm 40$ Re) and, at the same time, Cluster was anywhere in the nightside magnetotail ($X \leq -5$ and Y_{GSM} within $\pm$ 15 Re). When this condition is fulfilled, there is potentially a magnetic connection between Cluster and the Moon. We assume that Fe ions sputtered off the lunar surface are magnetized, and thus confined to the magnetic flux tube it was sputtered into. These would then be able to travel Earthward and potentially be detected by Cluster in the nightside magnetosphere. For these intervals, we then calculated an occurrence rate as described in section 2.3 for the years 2002–2018.

As a comparison, we also calculated a similar occurrence rate when the Moon was outside the magnetosphere. If lunar sputtering is modulated by the solar wind, one would expect a higher sputtering activity outside the magnetosphere, but the magnetic connectivity to Cluster does not exist (or cannot be established), and Cluster should detect fewer Fe ions. As the moon traverses the magnetotail within a few days, there are obviously far more observations during non-moon-in-magnetotail periods.

A comparison between Fe detection rates during these two conditions did not give any meaningful results, however, so while the Moon may be a source of the Fe we detect with RAPID, we are not able to quantify this contribution with our data set.

4.2. Fe Observations During Recurring Meteor Swarms

A key element in Christon et al. (2017) was the relation between ablation of meteors, the subsequent deposition of metallic atoms in the mesosphere and thereafter outflow to the magnetosphere. Based on rocket experiments (e.g., Istomin, 1963; Kopp, 1997), the mean total column density of metal ions (Fe^+, Mg^+, Ca^+, Na^+; with Fe^+ being the dominant species) in the atmosphere is 4e−9 cm^{-3} without special meteor shower activity. During meteor showers, the density can increase significantly: During the Perseid meteor shower in 1976, Kopp (1997) reported an order of magnitude increase in the total columnal density, mainly due to enhanced Fe^+ deposition.

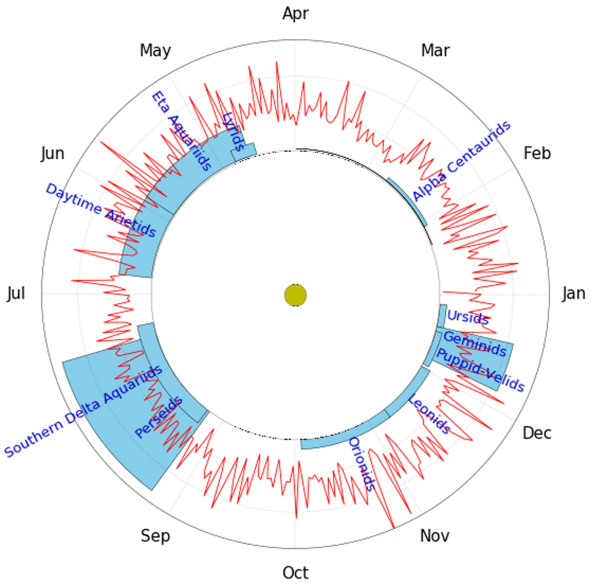

Meteor shower	Period	Rate
Perseids	17 Jul - 24 Aug	150
Geminids	4 Dec - 17 Dec	120
Quadrantids	28 Dec - 12 Jan	120
Eta Aquariids	19 Apr - 28 May	50
Daytime Arietids	14 May - 24 Jun	50
Southern Delta Aquariids	12 Jul - 23 Aug	25
Lyrids	16 Apr - 25 Apr	18
Leonids	6 Nov - 30 Nov	15
Orionids	2 Oct - 7 Nov	15
Puppid-Velids	1 Dec - 15 Dec	10
Ursids	17 Dec - 26 Dec	10
Alpha Centaurids	28 Jan - 21 Feb	6

Figure 7. Polar plot illustrating average Fe detection and meteor activity as the Earth orbits around the Sun. The blue bars show periods with enhanced meteor shower activity; the radius of these indicate the zenithal hourly rate, a measure of the meteor shower intensity (ranges from 6 to 150). Blue text shows the common names of the meteor swarms (listed to the right) plotted where the meteor showers have their peak zenithal hourly rate. The red line shows average daily Fe count (range 5 to 313) rate as a function of season (and thus the Earth's orbital phase).

Dust sized meteoroids are entering the atmosphere every few seconds, also when there is no notable meteor shower activity. The composition varies depending on the parent asteroid or comet originally responsible for their creation. Some of these leave visible trails in the sky. Spectroscopy can give detailed information about the composition, but as a rule of thumb, meteors creating yellowish (~ 570–590 nm wavelength) illumination in the night time sky is consistent with a high Fe content.

In addition to these continuously incoming dust particles, the Earth also regularly passes through larger meteoroid clouds during its travel around the Sun. These clouds are remnants of comets and asteroids that have passed the Earth's trajectory, and are encountered around the same time every year, that is, at certain segments of the Earth's orbit around the Sun as illustrated in Figure 7. We checked for possible correlations between Fe occurrence rates and the zeniths hourly rate (i.e., number of visible meteors streaking through the night sky) for 12 known recurring meteor swarms (Molau & Rendtel, 2009).

Figure 7 illustrates the location of these 12 major recurring meteor swarms, marked as blue bars along the Earth's yearly orbit around the Sun. The radius/height of the bars indicate the intensity of the swarms, given as Zenithal Hourly Rate (ZHR; see, e.g., MacRobert, 2012)—essentially the reported number of streaks visible from ground in the nightside sky within 1 hr. In terms of ZHR, the Perceids (peak occurence around 15 August) are the most prominent, followed by the Geminids (peak occurrence around 10 December) and the Quadrandids (peak occurrence around 8 January). The red curve along this trajectory shows the daily average Fe detection.

From the comparison of meteor swarm intensity and the number of RAPID DE detections illustrated in Figure 7, we do not see any striking correlations. A direct detection of any sputtering effects near the meteoroids (i.e., as Cluster fly through the meteor swarm), is thus not visible. The process of ablation, deposition and subsequent outflow as suggested by Christon et al. (2017) has much longer time scales; The deposited Fe ions can probably reside for a very long time in the mesosphere before eventually being lifted up and escape into space or deposited on Earth. Results by Raizada et al. (2015) (their Figure 10) suggest that Fe^+ have lifetimes up to 1,000 hr in the mesosphere).

5. Time Variations in the Fe Occurrence Ratio

The top panel of Figure 8 shows how the yearly number of Fe detections by Cluster 4 varies between 2001 and 2018. The overplotted blue line shows the monthly averages of the F10.7 index—a frequently used proxy

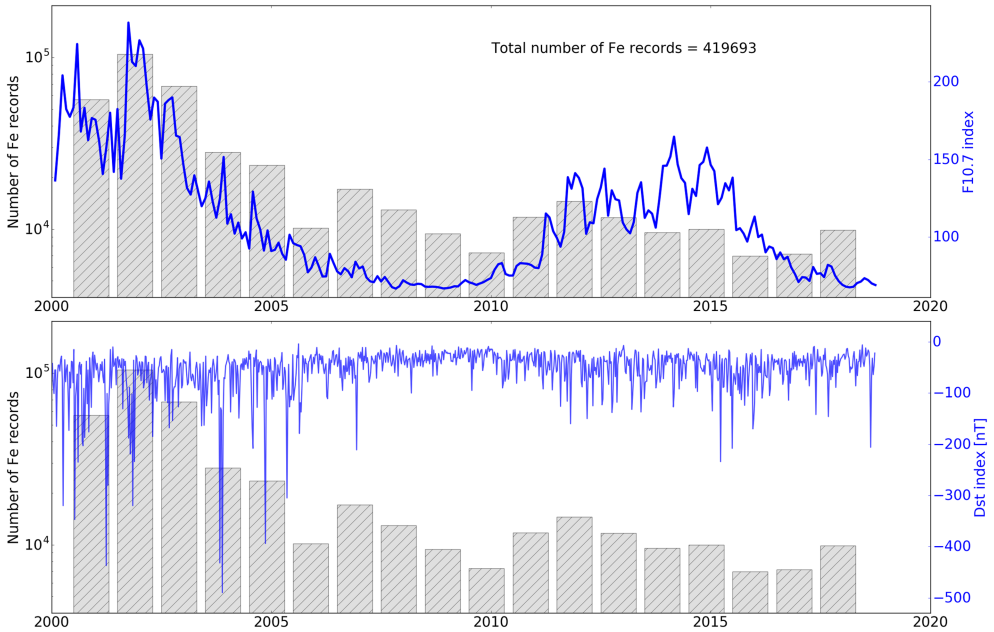

Figure 8. (top) Histogram showing number of Fe detections per year. Overplotted as a blue line is monthly averages of the F10.7 index—a proxy for solar activity. (bottom) Same statistics, but blue curve is now the minimum daily Dst index—a proxy for geomagnetic activity.

for solar activity. The two quantities seem to covary, but the Pearson linear correlation coefficient between them are only about 0.4. The highest Fe detection rates were detected during the initial period of Cluster, corresponding to maximum activity of solar cycle 22, followed by lower detection rates during solar minimum, and then increased detection rates toward solar maximum of solar cycle 23 again.

The lower panel in Figure 8 shows the same yearly number of Fe detections as bars, but this time overplotted the minimum daily Dst index—a proxy for geomagnetic activity. As seen, the highest geomagnetic activity (lower Dst) can be found in the early years when the solar activity was high.

We thus believe that the long term variation in the Fe detection is primarily a consequence of higher geomagnetic activity and thus more energization enabling detection by RAPID rather than a real solar cycle modulation of Fe abundance in geospace. Some of the long time variation may be skewed by sensor degradation over time, but since DE is a diagnostics product, no correction for this degradation has been made.

6. Summary

We have utilized the Direct Event (DE) diagnostics product from the RAPID instruments on board the Cluster satellites to investigate the presence of Fe ions in geospace. The DE product provides full energy and time of flight for a limited number of particles each spin period. From this information, the mass and thus the species of the incident ion can be determined. A prioritization scheme ensures that heavy ions are prioritized. Plotted in an energy versus time-of-flight map, Fe emerges as a pronounced and distinct population, so the identification of ions with atomic or molecular mass close to that of Fe is robust.

During the 18 years of observations, approximately 122,000 hr of DE data from Cluster SC4 were analyzed in detail. On average, Fe is detected during 9.1% of the observation time. The lower energy threshold for Fe detection is approximately 400keV, so there may be an addidional, less energetic hidden Fe poplulation.

We are not able to say anything about charge state, and thus the origin of the detected Fe ions. Due to the limited number of DE events per spin and the prioritization scheme, we are not able to calculate fluxes or even ratios between different species from the measurements. Still, by normalizing the time when Fe is observed to the total observation time, we are able to estimate an Fe occurrence rate. These results show that Fe is abundant in all regions of geospace covered by Cluster. To our knowledge, this paper is the first report on Fe abundance in geospace based on Cluster data.

The highest Fe occurrence rates can be found in the inner magnetosphere and tail plasma sheet, where Fe is detected 30% respectively 15% of the observation time. In the upstream solar wind and bow shock region traversed by Cluster, we observe Fe around 6% of the time. The occurrence rates are much lower in the high-latitude polar cap (including the cusps) and magnetically connected magnetotail lobe regions. Here we only observe Fe during 1–2 % of the observation time.

The difference in occurrence rate between the regions can partially be explained by instrument energy threshold; In the solar wind and plasma sheet, the ram velocity with respect to the spacecraft frame velocity provides the Fe ions with a significant part of the energy needed to be detected by the RAPID instrument. In the plasma sheet and inner magnetosphere, it is reasonable to assume that known heating mechanisms such as betatron acceleration, Fermi acceleration, and other adiabatic acceleration mechanisms as well as stochastic acceleration during substorms and bursty bulk flow events energize Fe ions sufficiently to be detected by RAPID. In the polar cap and lobe regions, none of these energization processes are very effective.

The occurrence rates and absolute Fe ion counts both show correlation with solar activity and geomagnetic activity. More Fe was detected during the initial period of Cluster, corresponding to maximum activity of solar cycle 22, followed by lower detection rates during solar minimum, and then increased detection rates toward solar maximum of solar cycle 23. We think that this result is primarily a consequence of higher geomagnetic activity and thus more energization, enabling detection by RAPID with its rather high-energy threshold, rather than a real solar cycle modulation of Fe abundance in geospace. Some of the long time variation may be skewed by sensor degradation over time, but since DE is a diagnostics product, no correction for this degradation has been made.

Since we are unable to determine charge state, we are also unable to identify the source of the observed Fe ions. It is reasonable to assume that most of the Fe ions detected in the solar wind are of solar origin and thus of high charge states. The detection of Fe ions in the high altitude polar cap region and the magnetically connected magnetotail lobes may support the results in Christon et al. (2017), in which single ionized Fe^{+} were extracted from mesospheric metallic layers formed by meteorite ablation. However, it is hard to reconcile how these ions can be locally accelerated to the energy threshold of the RAPID DE mode by classic outflow mechanisms. We thus suspect that the Fe detected by RAPID in the polar cap and lobe regions are part of the high-energy tail of a solar wind distribution of Fe that have entered through the magnetopause possibly through a mechanism similar to the Cusp Energetic Particle events described in Chen et al. (1998). If there is a ionospheric source of Fe^{+}, they will need to be energized and heated, for example in the tail plasma sheet or inner magnetosphere before they can be detected by RAPID.

Investigation of sputtering off asteroids or the lunar surface did not provide any conclusive results. Once again, any sputtered Fe ions present around asteroids or the Moon probably have too low energy to be detected with the RAPID IIMS detector.

Appendix A: Data Sources

All the Cluster data, including the RAPID DE mode data, are available from the Cluster Science Archive (https://www.cosmos.esa.int/web/csa). The data format (as well as comprehensive information about the RAPID instrument) is described in Daly and Kronberg (2019).

OMNI data used to check correlations with geomagnetic activity and solar illumination (F10.7) are available from the NASA Coordinated Data Analysis Web (CDAWeb: https://cdaweb.gsfc.nasa.gov/index.html).

Acknowledgments
Cluster RAPID was supported by the European Space Agency through the Cluster Science Archive activities and by the Deutsches Zentrum für Luft- und Raumfahrt (DLR) under Grant 50 OC 1602. I. Dandouras thanks CNES for its support to the Cluster project at IRAP. Cluster data, including the RAPID DE mode data, are available from the Cluster Science Archive (https://www.cosmos.esa.int/web/csa).

References

Abrahams, J. N. H., & Nimmo, F. (2019). Ferrovolcanism: Iron volcanism on metallic asteroids. *Geophysical Research Letters*, *46*, 5055–5064. https://doi.org//10.1029/2019GL082542

Agrell, S. O., Scoon, J. H., Muir, I. D., Long, J. V. P., McConnell, J. D. C., & Peckett, A. (1970). Mineralogy and petrology of some lunar samples:. *Science*, *167*(3918), 583. https://doi.org//10.1126/science.167.3918.583

Angelopoulos, V. (2008). The THEMIS mission. *Space Science Reviews*, *141*(1-4), 5–34. https://doi.org//10.1007/s11214-008-9336-1

Angelopoulos, V., Kennel, C. F., Coroniti, F. V., Pellat, R., Kivelson, M. G., Walker, R. J., & Gosling, J. T. (1994). Statistical characteristics of bursty bulk flow events. *Journal of Geophysical Research*, *99*(A11), 21,257–21,280. https://doi.org//10.1029/94JA01263

Asbridge, J. R., Bame, S. J., & Strong, I. B. (1968). Outward flow of protons from the Earth's bow shock. *Journal of Geophysical Research*, *73*(17), 5777–5782. https://doi.org//10.1029/JA073i017p05777

Bame, S. J., Asbridge, J. R., Hundhausen, A. J., & Montgomery, M. D. (1970). Solar wind ions: $^{56}Fe^{+8}$ to $^{56}Fe^{+12}$, $^{28}Si^{+7}$, $^{28}Si^{+8}$, $^{28}Si^{+9}$, and $^{16}O^{+6}$. *Journal of Geophysical Research*, *75*(31), 6360. https://doi.org//10.1029/JA075i031p06360

Banks, P. M., & Holzer, T. E. (1968). The polar wind. *Journal of Geophysical Research*, *73*(21), 6846–6854. https://doi.org//10.1029/JA073i021p06846

Baron, R. L., Bilson, E., Gold, T., Colton, R. J., Hapke, B., & Steggert, M. A. (1977). The surface composition of lunar soil grains: A comparison of the results of Auger and X-ray photoelectron (ESCA) spectroscopy. *Earth and Planetary Science Letters*, *37*(2), 263–272. https://doi.org//10.1016/0012-821X(77)90172-8

Baumjohann, W., Paschmann, G., Sckopke, N., Cattell, C. A., & Carlson, C. W. (1988). Average ion moments in the plasma sheet boundary layer. *Journal of Geophysical Research*, *93*(A10), 11,507–11,520. https://doi.org//10.1029/JA093iA10p11507

Baumjohann, W. (1998). Ion and electron heating in the near-Earth magnetotail. *Washington DC American Geophysical Union Geophysical Monograph Series*, *105*, 97. https://doi.org//10.1029/GM105p0097

Baumjohann, W., Paschmann, G., & Cattell, C. A. (1989). Average plasma properties in the central plasma sheet. *Journal of Geophysical Research*, *94*(A6), 6597–6606. https://doi.org//10.1029/JA094iA06p06597

Boakes, P., Nakamura, R., Volwerk, M., & Milan, S. (2014). ECLAT Cluster spacecraft magnetotail plasma region identifications (2001–2009). *Dataset Papers in Science*, *2014*, 1–13. https://doi.org//10.1155/2014/684305

Bochsler, P., Lee, M. A., Karrer, R., Popecki, M. A., Galvin, A. B., Kistler, L. M., & Opitz, A. (2010). Kinetic temperatures of iron ions in the solar wind observed with STEREO/PLASTIC. In *Twelfth International Solar Wind Conference* (M. Maksimovic, K. Issautier, N. Meyer-Vernet, M. Moncuquet, & F. Pantellini, Eds.), *1216*, pp. 257–260. https://doi.org//10.1063/1.3395850

Chappell, C. R., Moore, T. E., & Waite, J. (1987). The ionosphere as a fully adequate source of plasma for the Earth's magnetosphere. *Journal of Geophysical Research*, *92*(A6), 5896–5910. https://doi.org//10.1029/JA092iA06p05896

Chen, J., Fritz, T. A., Sheldon, R. B., Spence, H. E., Spjeldvik, W. N., Fennell, J. F., & Gurnett, D. A. (1998). Cusp energetic particle events: Implications for a major acceleration region of the magnetosphere. *Journal of Geophysical Research*, *103*(A1), 69–78. https://doi.org//10.1029/97JA02246

Christon, S. P., Hamilton, D. C., Mitchell, D. G., Plane, J. M., & Nylund, S. R. (2019). Suprathermal magnetospheric atomic and molecular heavy ions at and near Earth, Jupiter, and Saturn: Observations and identification. *Journal of Geophysical Research: Space Physics*, *24*, e2019JA027271. https://doi.org//10.1029/2019JA027271

Christon, S. P., Hamilton, D. C., Plane, J. M. C., Mitchell, D. G., Grebowsky, J. M., Spjeldvik, W. N., & Nylund, S. R. (2017). Discovery of suprathermal ionospheric origin Fe^{+} in and near Earth's magnetosphere. *Journal of Geophysical Research: Space Physics*, *22*, 11,175–11,200. https://doi.org//10.1002/2017JA024414

Chu, X., Yu, Z., Gardner, C. S., Chen, C., & Fong, W. (2011). Lidar observations of neutral Fe layers and fast gravity waves in the thermosphere (110–155 km) at McMurdo, Antarctica. *Geophysical Research Letters*, *38*, L23807. https://doi.org//10.1029/2011GL050016

Cladis, J. B. (1986). Parallel acceleration and transport of ions from polar ionosphere to plasma sheet. *Geophysical Research Letters*, *13*(9), 893–896. https://doi.org//10.1029/GL013i009p00893

Colaprete, A., Sarantos, M., Wooden, D. H., Stubbs, T. J., Cook, A. M., & Shirley, M. (2016). How surface composition and meteoroid impacts mediate sodium and potassium in the lunar exosphere. *Science*, *351*, 249–252. https://doi.org//10.1126/science.aad2380

Daly, P. W., & Kronberg, E. A. (2019). User guide to the RAPID measurements in the Cluster Science Archive (CSA), version 5.4.

Dandouras, I., Poppe, A. R., Fillingim, M. O., Kistler, L. M., Mouikis, C. G., Réme, H., & Parks, G. K. (2019). First simultaneous detection of terrestrial ionospheric heavy ions in the Earth's inner magnetosphere and at the Moon. *Nature Communications*, *11*, 8688.

Eastwood, J. P., Hietala, H., Toth, G., Phan, T. D., & Fujimoto, M. (2015). What controls the structure and dynamics of Earth's magnetosphere? *Space Science Reviews*, *188*(1-4), 251–286. https://doi.org//10.1007/s11214-014-0050-x

Ebihara, Y., & Ejiri, M. (2003). Numerical simulation of the ring current: Review. *Space Science Reviews*, *105*(1), 377–452. https://doi.org//10.1023/A:1023905607888

Escoubet, C. P., Schmidt, R., & Goldstein, M. L. (1997). Cluster—Science and mission overview. *Space Science Reviews*, *79*, 11–32. https://doi.org//10.1023/A:1004923124586

Fairfield, D. H. (1971). Average and unusual locations of the Earth's magnetopause and bow shock. *Journal of Geophysical Research*, *76*(28), 6700. https://doi.org//10.1029/JA076i028p06700

Fritz, T. A., Zurbuchen, T. H., Gloeckler, G., Hefti, S., & Chen, J. (2003). The use of iron charge state changes as a tracer for solar wind entry and energization within the magnetosphere. *Annales Geophysicae*, *21*(11), 2155–2164. https://doi.org//10.5194/angeo-21-2155-2003

Galvin, A. B., Ipavich, F. M., Gloeckler, G., Coplan, M., Hovestadt, D., Hilchenbach, M., & Verigin, M. I. (1996). Solar wind composition: First results from SOHO and future expectations. American Astronomical Society Meeting Abstracts #188 p. 49.05.

Galvin, A., Popecki, M., Simunac, K. D. C., Kistler, L., Ellis, L., Barry, J., & Wurz, P. (2009). Solar wind ion trends and signatures: STEREO PLASTIC observations approaching solar minimum. *Annales Geophysicae*, *27*, 3909–3922. https://doi.org//10.5194/angeo-27-3909-2009

Geiss, J., Bühler, F., Cerutti, H., Eberhardt, P., Filleux, C., Meister, J., & Signer, P. (2004). The Apollo SWC Experiment: Results, conclusions, consequences. *Space Science Reviews*, *110*(3), 307–335. https://doi.org//10.1023/B:SPAC.0000023409.54469.40

Grevesse, N. (1984). Accurate atomic data and solar photospheric spectroscopy. *Physica Scripta Volume T*, *8*, 49–58. https://doi.org//10.1088/0031-8949/1984/T8/008

Haaland, S., Lybekk, B., Svenes, K., Pedersen, A., Förster, M., Vaith, H., & Torbert, R. (2009). Plasma transport in the magnetotail lobes. *Annales Geophysicae*, *27*(9), 3577–3590. https://doi.org//10.5194/angeo-27-3577-2009

Hapke, B. (1973). Darkening of silicate rock powders by solar wind sputtering. *Moon*, *7*(3-4), 342–355. https://doi.org//10.1007/BF00564639

Heidrich-Meisner, V., Peleikis, T., Kruse, M., Berger, L., & Wimmer-Schweingruber, R. (2016). Observations of high and low Fe charge states in individual solar wind streams with coronal-hole origin. *Astronomy and Astrophysics*, *593*, A70. https://doi.org//10.1051/0004-6361/201527998

Hoshino, M., Saito, Y., Mukai, T., Nishida, A., Kokubun, S., & Yamamoto, T. (1997). Origin of hot and high speed plasmas in plasma sheet: Plasma acceleration and heating due to slow shocks. *Advances in Space Research*, *20*(4-5), 973–982. https://doi.org//10.1016/S0273-1177(97)00505-X

Hultqvist, B., & Øieroset, M. (1997). *Transport across the boundaries of the magnetosphere*. Dordrecht, the Netherlands: Kluwer Academic Publishers.

Hultqvist, B., & Stenflo, L. (1975). Physics of the hot plasma in the magnetosphere: [proceedings].

Istomin, V. G. (1963). Absolute concentrations of ion components of the Earth's atmosphere at altitudes between 100 and 200 km. *Planetary and Space Science*, *11*(2), 169–172. https://doi.org//10.1016/0032-0633(63)90139-9

Jarosewich, E. (1990). Chemical analyses of meteorites: A compilation of stony and iron meteorite analyses. *Meteoritics*, *25*(4), 323. https://doi.org//10.1111/j.1945-5100.1990.tb00717.x

Kopp, E. (1997). On the abundance of metal ions in the lower ionosphere. *Journal of Geophysical Research*, *102*(A5), 9667–9674. https://doi.org//10.1029/97JA00384

Korotev, R. L. (1997). Some things we can infer about the Moon from the composition of the Apollo 16 regolith. *Meteoritics and Planetary Science*, *32*, 447–478. https://doi.org//10.1111/j.1945-5100.1997.tb01291.x

Kronberg, E. A., Ashour-Abdalla, M., Dandouras, I., Delcourt, D. C., Grigorenko, E. E., Kistler, L. M., & Zelenyi, L. M. (2014). Circulation of heavy ions and their dynamical effects in the magnetosphere: Recent observations and models. *Space Science Reviews*, *184*(1-4), 173–235. https://doi.org//10.1007/s11214-014-0104-0

Kuhlman, K. R., Sridharan, K., & Kvit, A. (2015). Simulation of solar wind space weathering in orthopyroxene. *Planetary and Space Science*, *115*, 110–114. https://doi.org//10.1016/j.pss.2015.04.003

Laakso, H., Perry, C., McCaffrey, S., Herment, D., Allen, A. J., Harvey, C. C., & Turner, R. (2010). Cluster active archive: Overview. *Astrophysics and Space Science Proceedings*, *11*, 3–37. https://doi.org//10.1007/978-90-481-3499-1_1

Lundin, R., & Guglielmi, A. (2006). Ponderomotive forces in cosmos. *Space Science Reviews*, *127*(1), 1–116. https://doi.org//10.1007/s11214-006-8314-8

Lyons, L. R., & Speiser, T. W. (1982). Evidence for current sheet acceleration in the geomagnetic tail. *Journal of Geophysical Research*, *87*(A4), 2276–2286. https://doi.org//10.1029/JA087iA04p02276

MacRobert, A. (2012). Advanced meteor observing. Sky and Telescope.

Manuel, O. K., & Hwaung, G. (1983). Solar abundances of the elements. *Meteoritics*, *18*(3), 209. https://doi.org//10.1111/j.1945-5100.1983.tb00822.x

McIlwain, C. E. (1974). Substorm injection boundaries. In B. M. McCormac (Ed.), *Magnetospheric physics* (vol. 44, pp. 143). Dordrecht: Springer. https://doi.org//10.1007/978-94-010-2214-9_12

Mitchell, D. G., Roelof, E. C., & Bame, S. J. (1983). Solar wind iron abundance variations at speeds $>$ 600 km s^{-1}, 1972–1976. *Journal of Geophysical Research*, *88*(A11), 9059–9068. https://doi.org//10.1029/JA088iA11p09059

Molau, S., & Rendtel, J. (2009). A comprehensive list of meteor showers obtained from 10 years of observations with the IMO Video Meteor Network. *WGN, Journal of the International Meteor Organization*, *37*, 98–121.

Nakamura, E., Makishima, A., Moriguti, T., Kobayashi, K., Tanaka, R., Kunihiro, T., & Kawaguchi, J. (2012). Space environment of an asteroid preserved on micrograins returned by the Hayabusa spacecraft. *Proceedings of the National Academy of Sciences*, *109*(11), E624–E629. https://doi.org//10.1073/pnas.1116236109

Neugebauer, M. (1981). Observations of solar-wind helium. *Fundamentals of Cosmic Physics*, *7*, 131–199.

Nilsson, H., Waara, M., Marghitu, O., Yamauchi, M., Lundin, R., Rème, H., & Korth, A. (2008). An assessment of the role of the centrifugal acceleration mechanism in high altitude polar cap oxygen ion outflow. *Annales Geophysicae*, *26*(1), 145–157. https://doi.org//10.5194/angeo-26-145-2008

Paschmann, G., Papamastorakis, I., Sckopke, N., Haerendel, G., Sonnerup, B. U. O., Bame, S. J., & Elphic, R. C. (1979). Plasma acceleration at the Earth's magnetopause—Evidence for reconnection. *Nature*, *282*, 243–246. https://doi.org//10.1038/282243a0

Pillinger, C. T., Gardiner, L. R., & Jull, A. J. T. (1976). Preferential sputtering as a method of producing metallic iron, inducing major element fractionation and trace element enrichment. *Earth and Planetary Science Letters*, *33*(2), 289–299. https://doi.org//10.1016/0012-821X(76)90237-5

Plane, J. M. C. (1991). The chemistry of meteoric metals in the Earth's upper atmosphere. *International Reviews in Physical Chemistry*, *10*(1), 55–106. https://doi.org//10.1080/01442359109353254

Plane, J. M. C., Cox, R. M., & Rollason, R. J. (1999). Metallic layers in the mesopause and lower thermosphere region. *Advances in Space Research*, *24*(11), 1559–1570. https://doi.org//10.1016/S0273-1177(99)00880-7

Popova, O. P., Strelkov, A. S., & Sidneva, S. N. (2007). Sputtering of fast meteoroids surface. *Advances in Space Research*, *39*(4), 567–573. https://doi.org/10.1016/j.asr.2006.05.008

Poppe, A. R., Fillingim, M. O., Halekas, J. S., Raeder, J., & Angelopoulos, V. (2016). ARTEMIS observations of terrestrial ionospheric molecular ion outflow at the Moon. *Geophysical Research Letters*, *43*, 6749–6758. https://doi.org//10.1002/2016GL069715

Raizada, S., Tepley, C. A., Zhou, Q., Sarkhel, S., Mathews, J., Aponte, N. A., & Cabassa, E. (2015). Dependence of mesospheric Na and Fe distributions on electron density at Arecibo. *Earth, Planets, and Space*, *67*, 146. https://doi.org//10.1186/s40623-015-0322-z

Rakowski, C. E., & Laming, J. M. (2012). On the origin of the slow speed solar wind: Helium abundance variations. *The Astrophysical Journal*, *754*(1), 65. https://doi.org//10.1088/0004-637x/754/1/65

Rème, H., Aoustin, C., Bosqued, J. M., Dand ouras, I., Lavraud, B., Sauvaud, J. A., & Sonnerup, B. (2001). First multispacecraft ion measurements in and near the Earth's magnetosphere with the identical Cluster ion spectrometry (CIS) experiment. *Annales Geophysicae*, *19*, 1303–1354. https://doi.org//10.5194/angeo-19-1303-2001

Saito, Y., Yokota, S., Asamura, K., Tanaka, T., Nishino, M. N., Yamamoto, T., & Takahashi, F. (2010). In-flight performance and initial results of Plasma Energy Angle and Composition Experiment (PACE) on SELENE (Kaguya). *Space Science Reviews*, *154*(1-4), 265–303. https://doi.org//10.1007/s11214-010-9647-x

Seki, K., Elphic, R. C., Thomsen, M. F., Bonnell, J., McFadden, J. P., Lund, E. J., & Mukai, T. (2002). A new perspective on plasma supply mechanisms to the magnetotail from a statistical comparison of dayside mirroring O^+ at low altitudes with lobe/mantle beams. *Journal of Geophysical Research*, *107*(A4), 1047. https://doi.org//10.1029/2001JA900122

Shelley, E. G., Johnson, R. G., & Sharp, R. D. (1972). Satellite observations of energetic heavy ions during a geomagnetic storm. *Journal of Geophysical Research*, *77*(31), 6104. https://doi.org//10.1029/JA077i031p06104

Shi, Q. Q., Zong, Q. G., Fu, S. Y., Dunlop, M. W., Pu, Z. Y., Parks, G. K., & Lucek, E. (2013). Solar wind entry into the high-latitude terrestrial magnetosphere during geomagnetically quiet times. *Nature Communications*, *4*, 1466. https://doi.org//10.1038/ncomms2476

Sibeck, D. G., McEntire, R. W., Lui, A. T. Y., Lopez, R. E., Krimigis, S. M., Decker, R. B., & Potemra, T. A. (1987). Energetic magnetospheric ions at the dayside magnetopause: Leakage or merging? *Journal of Geophysical Research*, *92*(A11), 12,097–12,114. https://doi.org//10.1029/JA092iA11p12097

Slapak, R., Nilsson, H., Westerberg, L. G., & Larsson, R. (2015). O^+ transport in the dayside magnetosheath and its dependence on the IMF direction. *Annales Geophysicae*, *33*(3), 301–307. https://doi.org//10.5194/angeo-33-301-2015

Slapak, R., Schillings, A., Nilsson, H., Yamauchi, M., Westerberg, L. G., & Dand ouras, I. (2017). Atmospheric loss from the dayside open polar region and its dependence on geomagnetic activity: Implications for atmospheric escape on evolutionary timescales. *Annales Geophysicae*, *35*(3), 721–731. https://doi.org//10.5194/angeo-35-721-2017

Tanaka, T., Saito, Y., Yokota, S., Asamura, K., Nishino, M. N., Tsunakawa, H., & Terasawa, T. (2009). First in situ observation of the Moon-originating ions in the Earth's magnetosphere by MAP-PACE on SELENE (KAGUYA). *Geophysical Research Letters*, *36*, L22106. https://doi.org//10.1029/2009GL040682

Treumann, R. A. (1997). Theory of super-diffusion for the magnetopause. *Geophysical Research Letters*, *24*(14), 1727–1730. https://doi.org//10.1029/97GL01760

von Steiger, R., Geiss, J., & Gloeckler, G. (1997). Composition of the solar wind. Cosmic Winds and the Heliosphere p. 581.

von Steiger, R., Schwadron, N. A., Fisk, L. A., Geiss, J., Gloeckler, G., Hefti, S., & Zurbuchen, T. H. (2000). Composition of quasi-stationary solar wind flows from Ulysses/Solar Wind Ion Composition Spectrometer. *Journal of Geophysical Research*, *105*(A12), 27,217–27,238. https://doi.org//10.1029/1999JA000358

Wilken, B., Axford, W. I., Daglis, I., Daly, P., Guttler, W., Ip, W. H., & Ullaland, S. (1997). RAPID—The imaging energetic particle spectrometer on Cluster. *Space Science Reviews*, *79*, 399–473. https://doi.org//10.1023/A:1004994202296

Wilken, B., Daly, P. W., Mall, U., Aarsnes, K., Baker, D. N., Belian, R. D., & Zong, Q. G. (2001). First results from the RAPID imaging energetic particle spectrometer on board Cluster. *Annals of Geophysics*, *19*, 1355–1366. https://doi.org//10.5194/angeo-19-1355-2001

Wurz, P., Rohner, U., Whitby, J. A., Kolb, C., Lammer, H., Dobnikar, P., & Martín-Fernández, J. A. (2007). The lunar exosphere: The sputtering contribution. *Icarus*, *191*(2), 486–496. https://doi.org//10.1016/j.icarus.2007.04.034

Yamauchi, M., & Wahlund, J. E. (2007). Role of the ionosphere for the atmospheric evolution of planets. *Astrobiology*, *7*(5), 783–800. https://doi.org//10.1089/ast.2007.0140

Yau, A. W., & Andre, M. (1997). Sources of ion outflow in the high latitude ionosphere. *Space Science Reviews*, *80*, 1–25. https://doi.org//10.1023/A:1004947203046

Yau, A. W., Howarth, A., Peterson, W. K., & Abe, T. (2012). Transport of thermal-energy ionospheric oxygen (O^+) ions between the ionosphere and the plasma sheet and ring current at quiet times preceding magnetic storms. *Journal of Geophysical Research*, *117*, A07215. https://doi.org//10.1029/2012JA017803

Yau, A. W., Whalen, B. A., Goodenough, C., Sagawa, E., & Mukai, T. (1993). EXOS D (Akebono) observations of molecular NO^+ and N_2^+ upflowing ions in the high-altitude auroral ionosphere. *Journal of Geophysical Research*, *98*(A7), 11,205–11,224. https://doi.org//10.1029/92JA02019

Ziegler, J. F., Ziegler, M. D., & Biersack, J. P. (2010). SRIM—The stopping and range of ions in matter (2010). *Nuclear Instruments and Methods in Physics Research B*, *268*(11-12), 1818–1823. https://doi.org//10.1016/j.nimb.2010.02.091